Acta Geotechnica (2015) 10:343–355
DOI 10.1007/s11440-015-0381-0

RESEARCH PAPER

Mesh-free modeling of liquefaction around a pipeline under the influence of trench layer

Saman Soleimani Kutanaei[1] · **Asskar Janalizadeh Choobbasti**[1]

Received: 11 April 2013 / Accepted: 10 March 2015 / Published online: 28 March 2015

Abstract This paper reports numerical study of pore pressure evaluation and liquefaction potential around offshore buried pipelines by using the local radial basis function differential quadrature method. The current mesh-free method is a combination of differential quadrature approximation of derivatives and function approximation of MQ-radial basis function. A multilayer node distribution around a pipeline is used to obtain more accurate results in the area near the pipelines. Various physical parameters of the soil such as the permeability coefficient (k) and unit weight (γ) of the soil along with different shapes and locations of the trench layer are considered. The results are obtained in terms of liquefaction potential contours and pore pressure profiles. From the numerical aspect, the outcomes verify that the current technique is capable of solving different physical problems with complex geometries.

Keywords Buried pipeline · Liquefaction · Local RBF-DQ · Mesh-free method · Trench layer

1 Introduction

Today, a large part of population and industry are concentrated around the coast and more and more exploration activities take place in coastal area and offshore. Marine structures such as breakwaters, pipeline, oil drilling platforms, and wind turbines are constructed to protect coastal community, to facilitate marine transport, or to generate energy. One of the major factors of lifeline damage in earthquakes is horizontal ground displacement caused by liquefaction of loose granular soils, as illustrated in the case studies for many past earthquakes in the USA and Japan [18].

In case of deformation of water-saturated soil, the pressure of the water in the pores changes as the consequence of the change in additional external load. Analysis of soil under this condition is a complicated problem, involving not only the mechanical properties of soil skeleton but also the interaction with the pore water, which depends on the permeability of soil and the geometry of the soil volume. This condition is called "consolidation." In the extreme condition of undrained deformation, no movement of pore water with respect to the soil skeleton occurs and hardly any volume change is possible due to the large stiffness of the pore water. The tendency of volume change for the adjustment of soil particles under the applied load causes a corresponding change in the pore water pressure. In the case of a constant total mean pressure and undrained deformation leading to an increase in pore pressure, the effective pressure due to the interparticle forces is reduced and therefore the frictional resistance of the soil becomes less. The frictional resistance of the soil mass can reduce so much that almost the whole total stress is carried by the water. The extreme condition is often identified as the "liquefied" state of soil. The occurrence of this state may lead to the flow of the soil mass, which is usually catastrophic

Seismic performance of pipelines has been studied by Trautmann et al. [30] and Newmark and Hall [7]. Karamitros et al. [11] presented an analytical methodology to simulate buried pipeline behavior under permanent ground-induced actions. Sumer et al. [29] used wave tank to

---

✉ Saman Soleimani Kutanaei
samansoleimani16@yahoo.com

[1] Department of Civil Engineering, Babol University of Technology, P.O. Box 484, Babol, Iran

investigate sinking and floating of pipeline in liquefied sand. Zhiying [32] introduced the initial and boundary conditions to Terzaghi's one-dimensional consolidation equation containing pore pressure source term. Matsui [17] presented an analytical solution for a rigid pipeline in a semi-infinite seabed.

Due to the damages that may be caused by liquefaction as explained in the previous section, efforts have been developed to reduce the damage effects of this phenomenon. Of particular interest are efforts to densify the liquefiable soil and to provide drainage path to accelerate pore pressure dissipation during seismic loading by inclusion of column-like structure in the ground. Vibro-compaction, vibro-replacement, vibratory probe, and aggregate piers are some examples of ground improvement techniques that fit into this category.

Traditional numerical techniques such as finite difference, finite volume, and finite element methods (FDM, FVM, and FEM) are routinely used to solve complex problems. It is well known that these methods are strongly dependent on mesh properties. However, in solution of partial differential equations (PDEs) by these methods for complex geometries, mesh generation takes up very much time and is the most expensive part of the simulation. In light of difficulties of the meshing-related issues, various mesh-free methods have been developed. Among them are smooth particle hydrodynamics (SPH) [14], mesh-less local Petrov–Galerkin approach (MLPG) [24, 25], least-squares mesh-free method (LSMFM) [25, 31], etc. Recently, a new mesh-free method is proposed based on the so-called radial basis functions (RBFs) [6, 15]. Kansa [9, 10] introduced the direct collocation method using RBFs. To approximate derivatives by using RBFs, Shu and co-workers [5, 22] proposed the RBF-DQ method, which combines the differential quadrature (DQ) approximation [2, 23] of derivatives and function approximation of RBF. Previous applications [8, 12, 26–28] showed that RBF-DQ is an efficient method to solve linear and nonlinear PDEs and proved that the local radial basis function differential quadrature (local RBF-DQ) method is very flexible, simple in code writing and it can be easily applied to linear and nonlinear problems. In this method, the problem of ill-conditioned global matrix has been solved by replacement of global solvers with block partitioning schemes for large simulation problems as shown in Fig. 1.

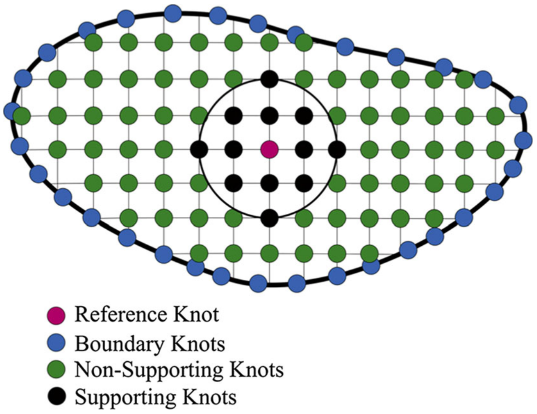

Fig. 1 Supporting knots around a centered knot

The main objective of the present work is to investigate the effects of different physical parameters such as permeability coefficient (k) and unit weight of the soil (γ) along with different shapes and locations of the trench layer on the liquefaction potential and pore pressure profiles. The mesh-free local RBF-DQ method is used for numerical simulation to obtain the desired parameters. A multilayer node distribution in the computational domain is used to reduce the computation time and to obtain accurate results around the pipe line.

2 Mathematical modeling and problem formulation

The physical model of the present work is shown in Fig. 2. The problem under consideration consists of a column of soil in porous seabed of finite thickness h containing a buried pipeline with radius r and surrounded by two impermeable walls.

2.1 Trench layer

In general, protection of a pipeline using a trench layer involves the following design parameters: (1) the fill-in materials and (2) configuration of the trench layer. In this work, the trench layer is simulated by assigning different properties for the trench layer. In the numerical simulation, higher permeability is used to mimic the behavior of the trench layer.

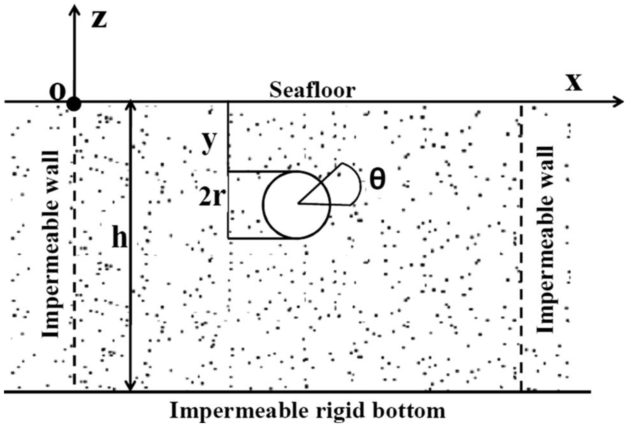

Fig. 2 Physical model of the present investigation

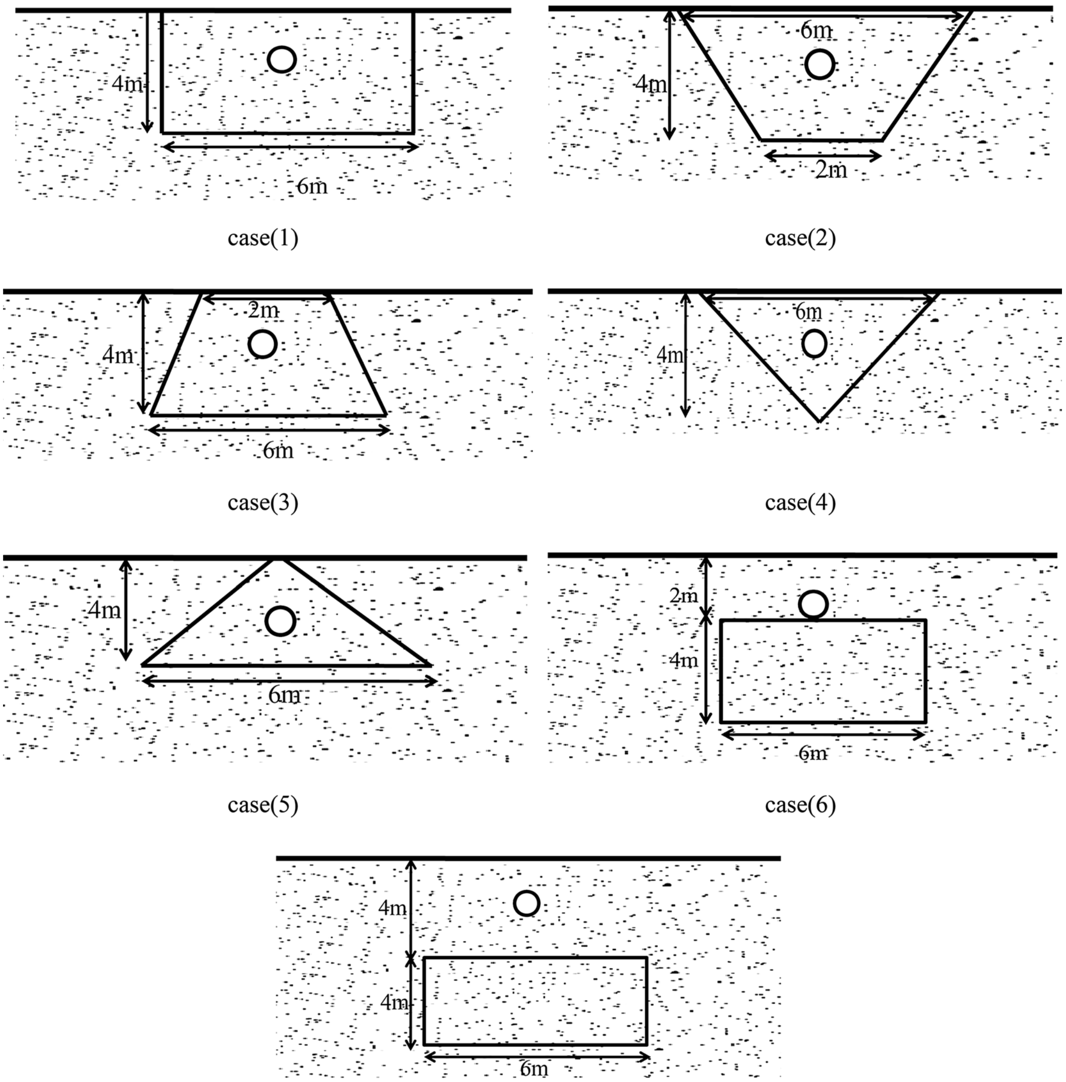

case(1)

case(2)

case(3)

case(4)

case(5)

case(6)

case(7)

Fig. 3 Different shapes and arrangements of the trench layer around the pipeline

In this parametric study, the local RBF-DQ is used for various shapes and locations of trench layers as shown in Fig. 3. The computational domain is the same for all cases which is a rectangle with length and width equal to 60 and 10 m, respectively. The center of pipeline is located at a fixed depth of 1.5 m under the soil and on the vertical center line of the domain.

2.2 Problem formulation

Based on Biot's consolidation theory [3], the equation of conservation for mass of saturated porous medium under two-dimensional plane strain condition is expressed as

$$\frac{\partial p}{\partial t} = \frac{k \times E \times K'}{\gamma_f [2(1-2v)(1+v)K' + n_s \times E]} \left(\frac{\partial^2 p}{\partial x^2} + \frac{\partial^2 p}{\partial z^2} \right) + f \tag{1}$$

where p is the pore pressure, γ_f the weight of pore water, k the permeability coefficient of soil, n_s the soil porosity, v is Poisson's ratio of the soil, K' the bulk modulus of pore fluid, and E the deformation modulus of the soil. Above f is the mean accumulative pore pressure source term.

2.3 Boundary conditions

For the physical model shown in Fig. 2, the boundary conditions in impermeable rigid bottom, impermeable boundaries, and the interfaces between soil particles and pipelines can be expressed as:

$$\begin{array}{lll} \dfrac{\partial p(x,-h;t)}{\partial z}=0 & & \text{On the bottom rigid boundary.} \\ \dfrac{\partial p(0,z;t)}{\partial x}=0 \quad \dfrac{\partial p(l,z;t)}{\partial x}=0 & & \text{For the impermeable boundaries.} \\ \dfrac{\partial p(x,z;t)}{\partial n}=0 \quad \text{for} \quad \sqrt{(x-x_0)^2+(z-z_0)^2}=r & & \text{On the pipeline walls.} \end{array} \tag{2a}$$

where l is the width of computation domain, x_0 and z_0 are the center coordinates of the pipeline, and n the outer normal direction of pipeline. The accumulative excess pore pressure for the sea surface is set to zero:

$$p(x,0;t)=0 \tag{2b}$$

and the initial condition can be expressed as:

$$p(x,z;0)=0 \tag{3}$$

2.4 Evaluating the accumulative excess pore pressure

Seed et al. [20] suggested the source term in seabed under seismic loading to be expressed as

$$f=\frac{\partial p_g}{\partial N}\frac{\partial N}{\partial t} \tag{4}$$

where $(\partial p_g/\partial N)$ is obtained by cyclic undrained tests. In Eq. 4, the relationship between p_g (accumulative excess pore pressure due to earthquake loading) and N (number of cycles of stress application) can be expressed as follows [19]:

$$\frac{\partial p_g}{\partial N}=\frac{\sigma_0'}{N_1} \tag{5}$$

where σ_0' denotes initial mean effective stress and N_1 is the number of uniform stress cycles required to cause liquefaction and expressed approximately as follows [19]:

$$N_1=\left[\frac{1}{\alpha}\frac{\tau_{eq}}{\sigma_0'}\right]^{\frac{1}{\beta}} \tag{6}$$

where α and β are the functions of soil type and relative density, generally $\alpha=0.246$, $\beta=-0.165$. Following the work of Seed et al. [20], the equivalent cyclic shearing stress τ_{eq} is expressed as follows:

$$\tau_{eq}=0.65\left(\frac{\gamma|z|}{g}\right)a_{\max}r_d \tag{7}$$

where z is the depth of calculation point to surface, g is the gravitational acceleration, $a_{\max}$ is the maximum ground acceleration, γ is the unit weight of soil, and r_d is the reduction coefficient of stress. $\partial N/\partial t$ in Eq. (4) is expressed as

$$\frac{\partial N}{\partial t}=\frac{N_{eq}}{t_d} \quad 0<t<t_d \tag{8a}$$

$$\frac{\partial N}{\partial t}=0 \quad t>t_d \tag{8b}$$

where t_d is the total duration of earthquake shaking and time is limited to t_d. N_{eq} is equivalent number of uniform load cycles for a given design earthquake [19]. The pore pressure source term can be expressed as

$$f=\frac{\partial}{\partial t}\left(\sigma_0'\frac{N}{N_1}\right)=\frac{\sigma_0'N_{eq}}{N_1t_d} \tag{9}$$

2.5 Numerical procedure

The local RBF-DQ method is described in this section. The present method is different from the conventional RBF-based collocation methods which are based on the function approximation [21]. The RBF-DQ method directly approximates the derivatives. Hence, it can be easily applied to the linear and nonlinear problems.

2.5.1 *Radial basis functions*

A radial basis function, denoted by $\varphi(\|x-x_j\|_2)$, is a continuous spline which depends on the separation distances of a subset of scattered points $x\in\Re^d$, in which d denotes the spatial dimension. The most commonly used RBF is

$$\text{Multiquadrics (MQ)}:\varphi(r)=\sqrt{r^2+c^2}, \quad c>0 \tag{10}$$

where $r=\|x-x_j\|_2$. For scattered points, the approximation of a function $f(x)$ can be written as a linear combination of H RBFs

$$f(x) \cong \sum_{j=1}^{H} \lambda_j \varphi\left(\left\|x - x_j\right\|_2\right) + \psi(x), \tag{11}$$

where H is the number of centers or knots $x, x = (x_1, x_2, \ldots x_d)$, d is the dimension of the problem, λ's are coefficients to be determined, and φ is the RBF. If Ψ_q^d denotes the space of d-variate polynomials of order not exceeding q, and letting the polynomials $p_1, \ldots, p_m$ be the basis of Ψ_q^d in $\Re^d$, then the polynomial $\psi(x)$, in Eq. (11), is usually written in the following form

$$\psi(x) = \sum_{i=1}^{m} \zeta_i P_i(x) \tag{12}$$

where $m = (q - 1 + d)!/(d!(q - 1)!)$. To determine the coefficients $(\lambda_1, \ldots, \lambda_H)$ and $(\zeta_1, \ldots, \zeta_m)$, extra m equations are required in addition to the H equations resulting from the collocating Eq. (11) at the H knots. This is insured by the m conditions for Eq. (11), that is

$$\sum_{j=1}^{H} \lambda_j P_i(x_j) = 0 \quad i = 1, \ldots, m. \tag{13}$$

2.5.2 *Differential quadrature method (DQ)*

The DQ method is a numerical discretization technique for approximation of derivatives which is initiated from the idea of conventional integral quadrature. The essence of the DQ method is that the partial derivative of an unknown function with respect to an independent variable can be approximated by a linear weighted sum of functional values at all mesh points in that direction. Suppose that a function $f(x)$ is sufficiently smooth. Then, its mth-order derivative with respect to x at a point x_i can be approximated by DQ as:

$$f_x^{(m)}(x_i) = \sum_{j=1}^{H} w_{ij}^{(m)} f(x_i), \quad i = 1, 2, \ldots, H, \tag{14}$$

where x_j are the discrete points in the domain, and $f(x_j)$ and $w_{ij}^{(m)}$ are the function values at these points and the related weighting coefficients, respectively. More detail can be found in [26–28].

2.5.3 *Local MQ-DQ method formulation*

In the local MQ-DQ method, the MQ RBFs are used as the basis functions to determine the weighting coefficients in the DQ approximation of derivatives for a two-dimensional problem [22]. However, the method can be easily extended to three-dimensional problems. Suppose that the solution of a partial differential equation is continuous, which can be approximated by MQ RBFs, and only a constant is included in the polynomial term $\psi(x)$, the function in the domain can be approximated by MQ RBFs as

$$f(x, y) = \sum_{j=1}^{H} \lambda_j \sqrt{(x - x_j)^2 + (y - y_j)^2 + c_j^2} + \lambda_{H+1} \tag{15}$$

To make the problem be well posed, one more equation is required. From Eq. (13), we have

$$\sum_{j=1}^{H} \lambda_j = 0 \Rightarrow \lambda_j = -\sum_{j=1, j \neq i}^{H} \lambda_j \tag{16}$$

Substituting Eq. (16) into Eq. (15) gives

$$f(x, y) = \sum_{j=1, j \neq i}^{H} \lambda_j g_j(x, y) + \lambda_{H+1} \tag{17}$$

where

$$\begin{aligned} g_j(x, y) = {} & \sqrt{(x - x_j)^2 + (y - y_j)^2 + c_j^2} \\ & - \sqrt{(x - x_i)^2 + (y - y_i)^2 + c_i^2} \end{aligned} \tag{18}$$

λ_{H+1} can be replaced by λ_i and Eq. (17) can be written as

$$f(x, y) = \sum_{j=1, j \neq i}^{H} \lambda_j g_j(x, y) + \lambda_i \tag{19}$$

$f(x, y)$ in Eq. (19) constitutes H-dimensional linear vector space V^H with respect to the operation of addition and multiplication. Substituting all the base functions into Eq. (18), we have

$$\sum_{k=1}^{H} w_{ik}^{(m)} = 0 \tag{20}$$

$$\begin{aligned} \frac{\partial g_j(x_i, y_i)}{\partial x} = {} & \sum_{k=1}^{H} w_{ik}^{(m)} g_j(x_k, y_k) - \frac{x - x_i}{\sqrt{(x - x_i)^2 + (y - y_i)^2 + c_i^2}} \\ & i = 1, \ldots, H, j \neq i \end{aligned} \tag{21}$$

For the given i, equation system (20, 21) has H unknowns with H equations. So, solving this equation system can obtain the weighting coefficient s$w_{ik}^{(m)}$. From Eq. (18), one can easily obtain the first-order derivative of $g_j(x, y)$ as

$$\begin{aligned} \frac{\partial g_j(x_i, y_i)}{\partial x} = {} & \frac{x - x_j}{\sqrt{(x - x_j)^2 + (y - y_j)^2 + c_j^2}} \\ & - \frac{x - x_i}{\sqrt{(x - x_i)^2 + (y - y_i)^2 + c_i^2}} \end{aligned} \tag{22}$$

In the matrix form, the weighting coefficient matrix of the x-derivative can then be determined by

$$[G][W^n]^T = \{G_x\} \tag{23}$$

where $[W^n]^T$ is the transpose of the weighting coefficient matrix $[W^n]$, and

$$[W^n] = \begin{bmatrix} w_{1,1}^{(n)} & w_{1,2}^{(n)} & \cdots & w_{1,H}^{(n)} \\ w_{2,1}^{(n)} & w_{2,2}^{(n)} & \cdots & w_{2,1}^{(n)} \\ \vdots & \vdots & \ddots & \vdots \\ w_{H,1}^{(n)} & w_{H,2}^{(n)} & \cdots & w_{H,H}^{(n)} \end{bmatrix},$$

$$[G] = \begin{bmatrix} 1 & 1 & \cdots & 1 \\ g_1(x_1,y_1) & g_1(x_2,y_2) & \cdots & g_1(x_H,y_H) \\ \vdots & \vdots & \ddots & \vdots \\ g_N(x_1,y_1) & g_N(x_2,y_2) & \cdots & g_H(x_H,y_H) \end{bmatrix} \quad (24)$$

$$[G_x] = \begin{bmatrix} 0 & 0 & \cdots & 0 \\ g_x^n(1,1) & g_x^n(1,2) & \cdots & g_x^n(1,H) \\ \vdots & \vdots & \ddots & \vdots \\ g_x^n(H,1) & g_x^n(H,2) & \cdots & g_x^n(H,H) \end{bmatrix}$$

With the known matrices $[G]$ and $[G_x]$, the weighting coefficient matrix of x-derivative $[W^n]$ can be obtained by using a direct or iterative method such as LU decomposition or SOR. The weighting coefficient matrix of the y-derivative can be obtained in a similar manner. More details can be found in Ref. [1, 4, 5, 13, 22, 23].

2.5.4 *Shape parameter (C) in local MQ-DQ method*

As mentioned before, the MQ approximation of the function contains a shape parameter C that could be knot dependent and must be determined by the user. In our study, C is chosen as a constant and is taken as 0.12, and the number of supporting knots is taken as 16 based on the previous work of Ding et al. [14].

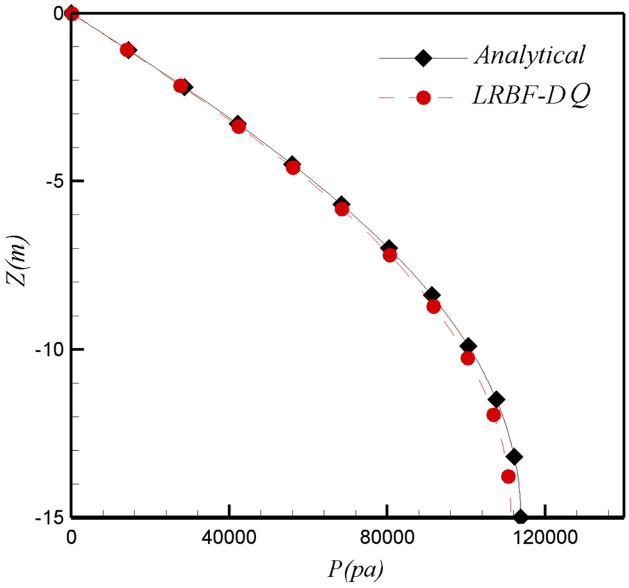

Fig. 4 Comparison of the obtained result from the present code with the analytical solution of Zhiying [32]

3 Numerical validation of the present code

To validate the present code, the results obtained by MQ-DQ model are compared with those of one-dimensional model. The governing equations for the one-dimensional model read [20]:

$$\frac{\partial p}{\partial t} - \frac{k \times E \times K'}{\gamma_f[2(1-2\nu)(1+\nu)K' + n_s \times E]}\left(\frac{\partial^2 p}{\partial z^2}\right) = \frac{\sigma_0' N_{eq}}{N_1 t_d}$$
$$0 < t < t_d \quad (24a)$$

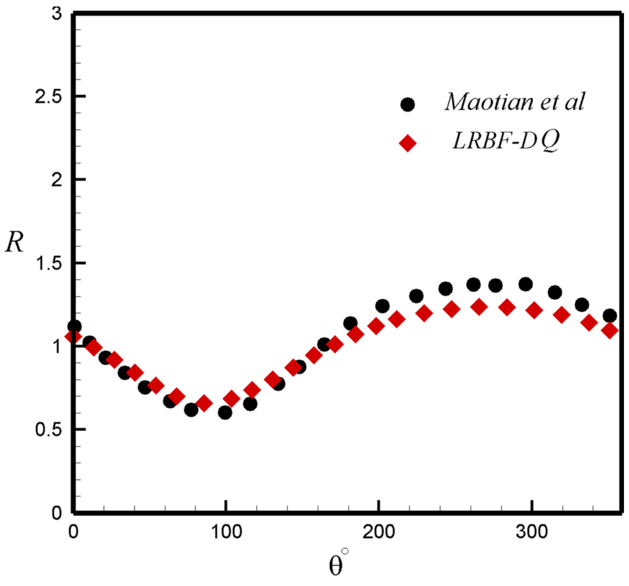

Fig. 5 Comparison of the present result with those obtained by Maotian et al. [16]

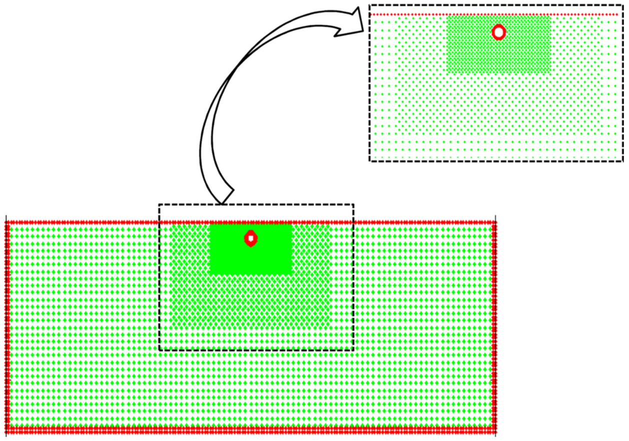

Fig. 6 Node distribution within the computational domain

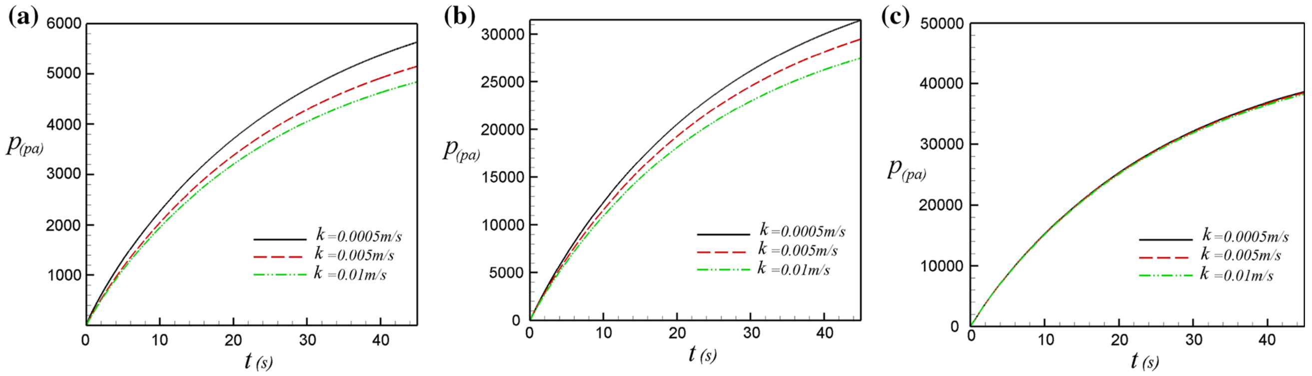

Fig. 7 Development of accumulative excess pore pressure for various permeability coefficients of soil (k) **a** at the top of the pipeline **b** at the bottom of the pipeline **c** at depth of 8 and 5 m from the pipe

$$\frac{\partial p}{\partial t}-\frac{k\times E\times K'}{\gamma_f[2(1-2v)(1+v)K'+n_s\times E]}\left(\frac{\partial^2 p}{\partial z^2}\right)=0\quad t>t_d \tag{24b}$$

The initial and boundary conditions for Eqs. (24a) and (24b) can be expressed as follows:

$$p(z,0)=0,\quad p(0,t)=0,\quad \frac{\partial p(-h,t)}{\partial z}=0 \tag{25}$$

Figure 4 shows the comparison of the obtained result with the analytical solution of Zhiying [32] for $a_{\max}=0.19\ g$, $N_{eq}=15$, $t_d=30\ s$, thickness of seabed $h=15$ m, unit weight of soil $\gamma_s=19$ kN/m^3 and porosity of soil $n_s=0.4$. The deformation modulus, permeability coefficient, and Poisson's ratio of soil are $E=50\times10^6$ Pa, $k=0.004$ m/s and $v=0.3$, respectively. As can be seen, the results are in an excellent agreement.

Moreover, the result of two-dimensional investigation obtained by Maotian et al. [16] is compared with the result of the present code in Fig. 5. The comparison indicates the acceptable agreement of them.

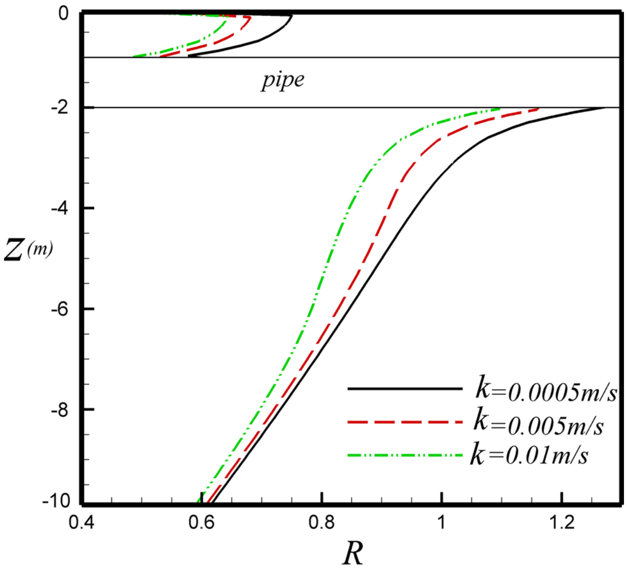

Fig. 8 Variation of R along the vertical centerline in the solution domain for different permeability of the trench layer

4 Results and discussion

To obtain an accurate result around the pipeline along and reducing the computational time, a multilayer node distribution is used in the computational domain as shown in Fig. 6. A serial test is carried out to obtain the appropriate number of nodes inside the computational domain. The independency of results from the number of the computational nodes is achieved for 4156 nodes inside the computational domain.

The constant parameters used for the numerical computations are: $a_{\max}=0.13\ g$, $N_{eq}=27$, $t_d=45\ s$. Thickness of seabed is $h=10$ m, and the porosity and unit weight of soil are $n_s=0.4$ and $\gamma_s=20$ kN/m^3. The deformation modulus, permeability coefficient and Poisson's ratio of soil are $E=70\times10^6$ Pa, $k=0.0002$ m/s, and $v=0.35$, respectively. The bulk modulus of pore fluid is $K'=2\times10^9$ Pa. The burial depth and radius of the pipeline are set to $y=1.5$ m and $r=0.5$ m. The liquefaction potential is defined as $R=p/\sigma_0'$ in this study, where $\sigma_0'=(\gamma_s-\gamma_f)\times z$ is the initial vertical effective stress of seabed and p is accumulative pore pressure induced by seismic loading [32]. The liquefaction occurred when $R>1$.

4.1 Effect of soil permeability of trench layer

Figure 7 shows the effect of trench layer's permeability on the accumulative excess pore pressure for case (1) with

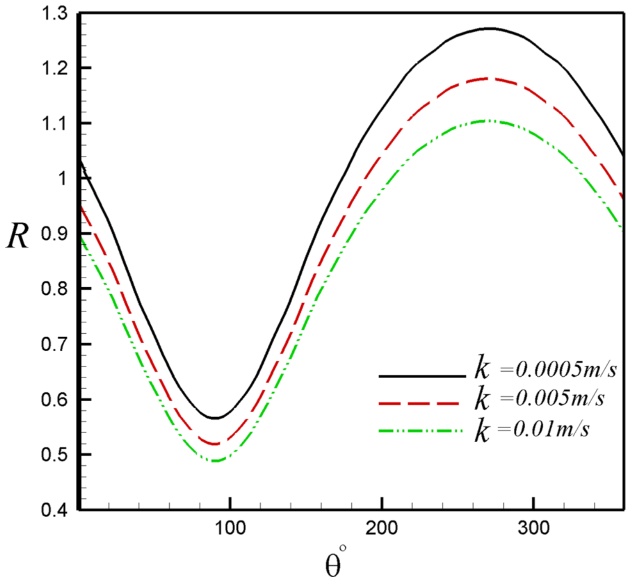

Fig. 9 Variation of R around the pipeline at various angular locations

depth ($d = 6$ m) and width ($b = 4$ m). The figure demonstrates that with increase in permeability, the accumulative excess pore pressure generation reduces. Moreover, Fig. 7c indicates that as the distance from the trench layer enhances, the effect of trench layer diminishes.

Variation of liquefaction potential (R) along the vertical centerline in the solution domain for different permeability of the trench layer is shown in Fig. 8. The figure clearly shows that as the distance from the trench layer increases, the liquefaction potential profiles approach together beneath the pipe, indicating the reduction in trench layer effect at these locations. In general, with growth of depth, R decreases considerably as the rate of increasing effective stress becomes greater than the rate of increasing accumulative excess pore pressure.

Figure 9 shows the variation of R around the pipeline at various angular locations. As seen, the maximum and minimum values of liquefaction potential occur at $\theta = 270$ and $\theta = 90°$, respectively. In addition, increase in the permeability coefficient causes the values of R to reduce.

4.2 Effect of unit weight of trench layer

Development of accumulative excess pore pressure for various unit weights of soil at the top and bottom of the pipeline is shown in Fig. 10a and b. This figure shows that increase in unit weight of the trench layer has no significant effect on the time–history curve of seismic accumulative excess pore pressure far away the pipeline. Figure 11 shows the liquefaction potential profiles for various values of γ_s along the vertical centerline of the computational domain. The figure indicates that adding a trench layer with higher unit weight has a significant effect on the decrease in liquefaction potential inside the trench area. This reduction is due to the increasing effective stress in the trench layer. It is worth mentioning that this effect becomes negligible outside the trench layer.

4.3 Effect of width (b) of trench layer

Variation of the accumulative excess pore pressure for various widths ($b = 4$, 5, 6 m) and a constant depth

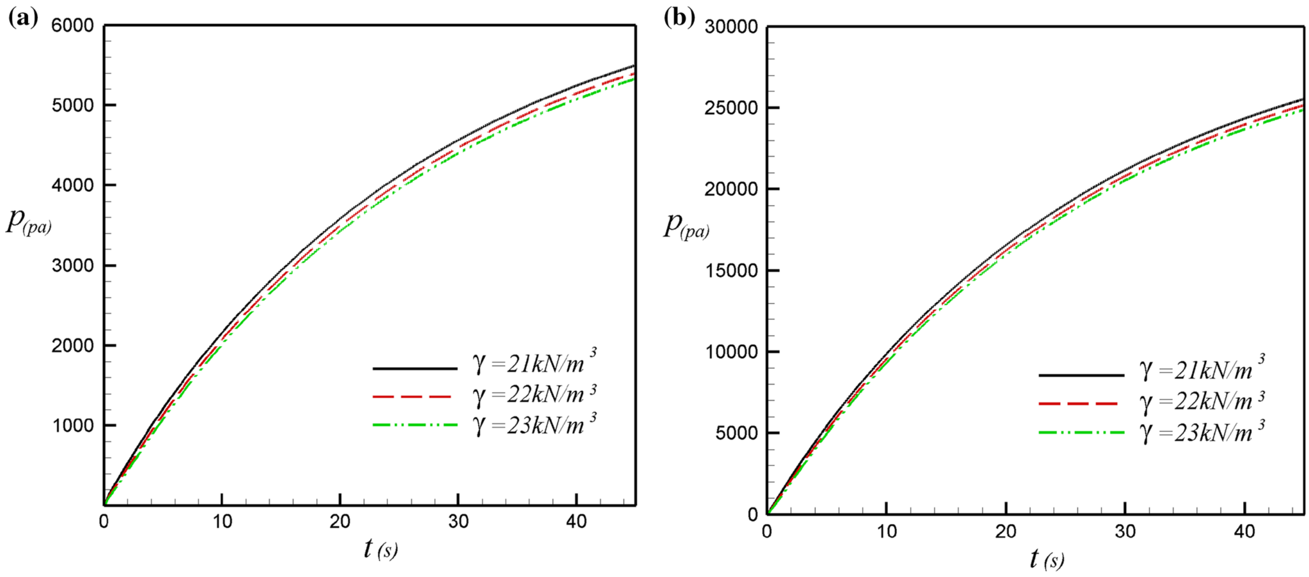

Fig. 10 Development of accumulative excess pore pressure for various unit weights of soil (γ_s); **a** at the top of the pipeline **b** at the bottom of the pipeline

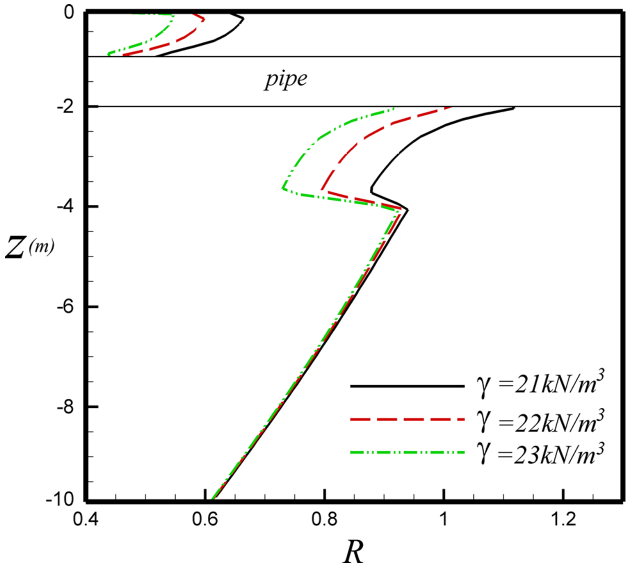

Fig. 11 Variation of R along the vertical centerline in the solution domain for different γ_s of the trench layer

($d = 4$ m) of rectangular trench layer (case 1) is shown in Fig. 12. It can be seen that the effect of b on the excess pore pressure is not considerable. Figure 13 also shows that the effect of trench layer width on the liquefaction potential is not considerable along the vertical axis.

4.4 Effect of depth (d) of trench layer

Figure 14 shows the effect of trench layer depth on the accumulative excess pore pressure for the trench layer width ($b = 6$ m) and different depths ($d = 4$, 5, 6 m) for case (1). The figure indicates that the effect of changing depth of trench layer is more considerable than the effect of trench layer's width. In addition, the growth of d decreases the accumulative excess pore pressure at the top and bottom of the pipeline. As can be seen in Fig. 15, effect of increasing the trench layer depth on the reduction in liquefaction potential area is greater than the effect of the trench layer's width on that. Contrary to the effect of trench layer width, as the depth of trench layer increases, the

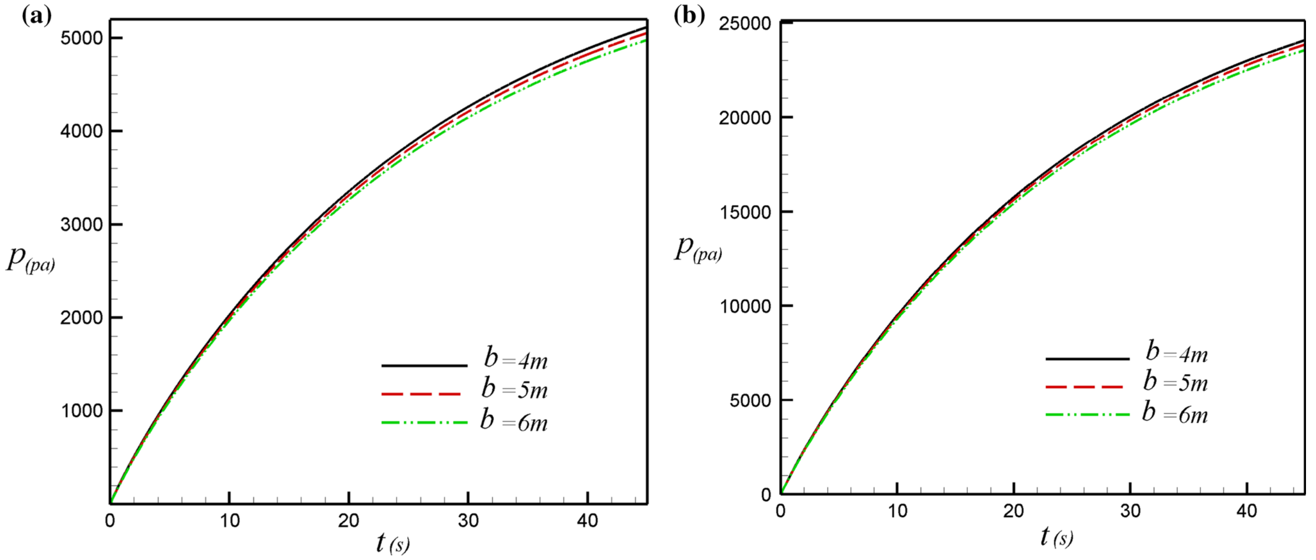

Fig. 12 Development of accumulative excess pore pressure for various widths of rectangular trench layer; **a** at the top of the pipeline **b** at the bottom of the pipeline

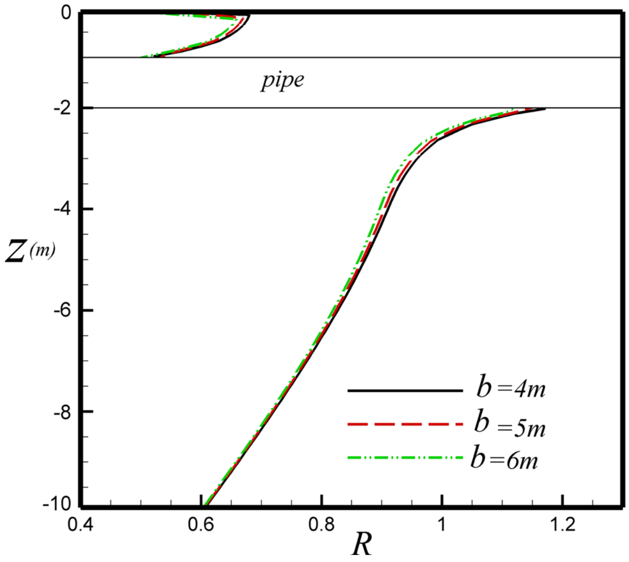

Fig. 13 Variation of R along the vertical centerline in the solution domain for different trench layer widths

liquefied area around the pipeline reduces noticeably and disappears at $d > 5$ m.

The comparison of the accumulative excess pore pressure for a triangular trench layer with the base length of 6 m and height of 4 m is shown in Fig. 16. The comparison is carried out for two different arrangements: case (4) and case (5). These profiles indicate that case (5) where the base of the triangle is located at the deeper location of seabed causes less accumulative excess pore pressure.

Comparison of R for two arrangements of trapezoidal trench layer of cases (2) and (3) is shown in Fig. 17. The result is similar to the triangular trench layer case, but the difference between these two cases are much less than those of cases (4) and (5).

4.5 Effect of the trench layer location

Effects of different locations of the rectangular trench layer on the accumulative liquefaction potential and liquefied

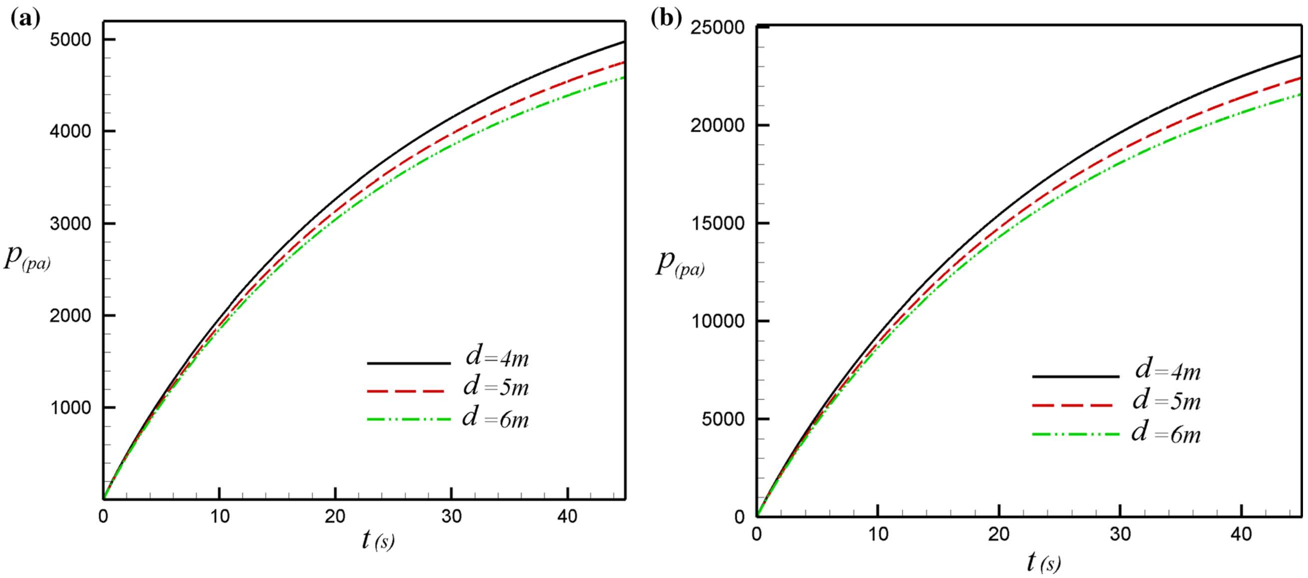

Fig. 14 Development of accumulative excess pore pressure for $b = 6$ m and various depths of rectangular trench layer; **a** at the top of the pipeline **b** at the bottom of the pipeline

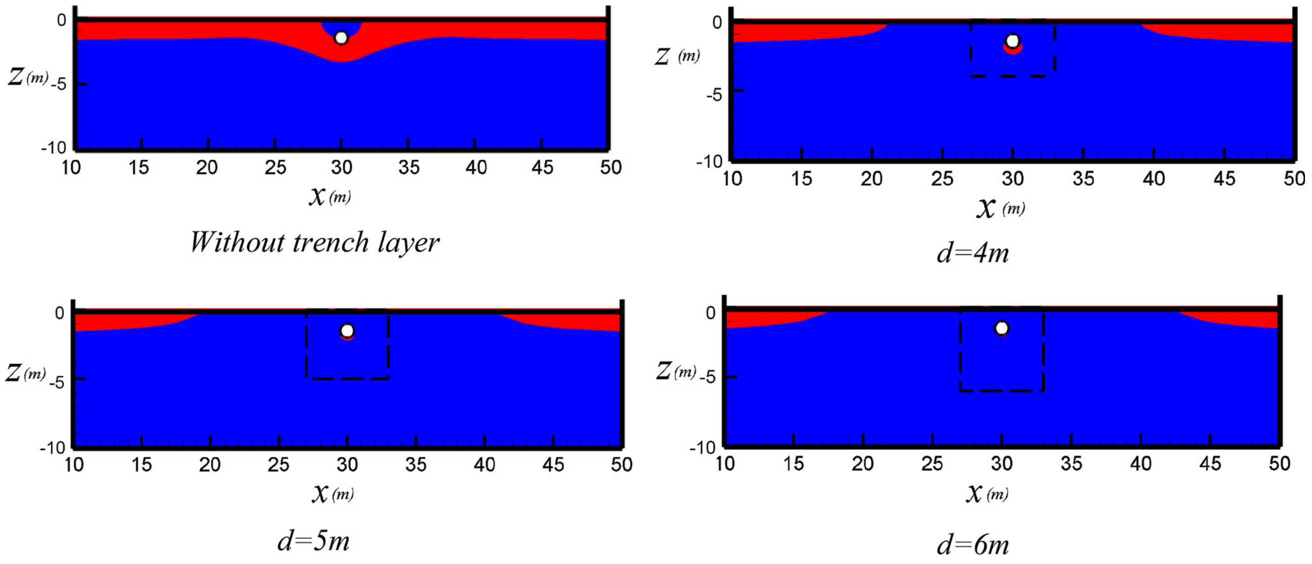

Fig. 15 Countor of liquefaction of soil for various values of depth (d) of trench layer around pipeline

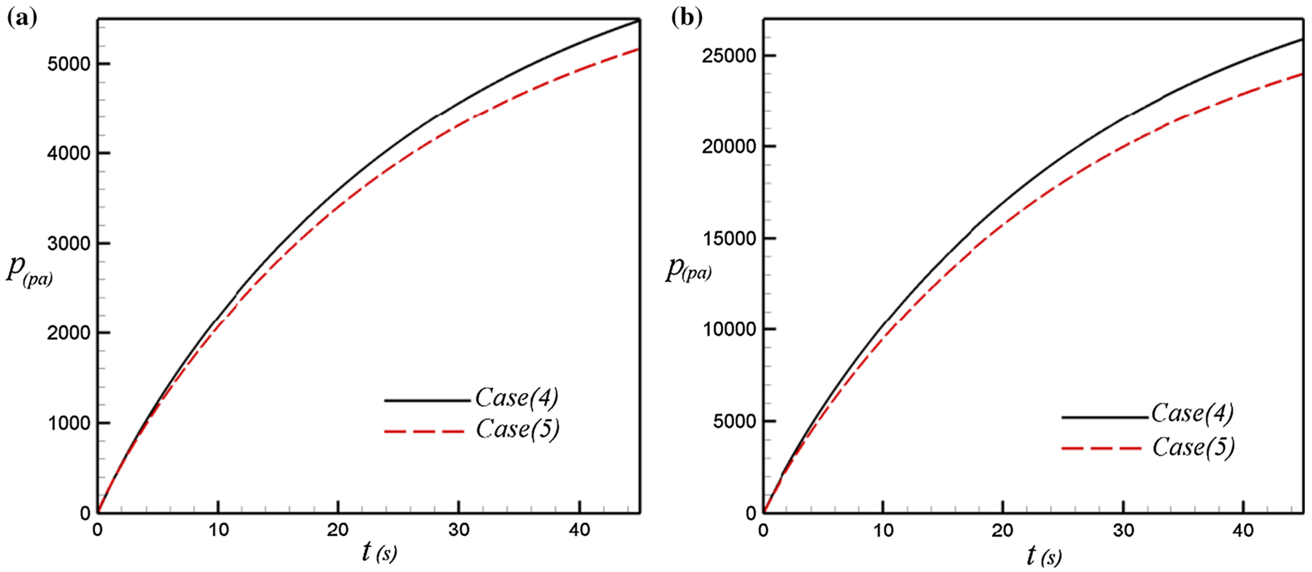

Fig. 16 Comparision of the accumulative excess pore pressure at during seismic loading for the triangular trench layer **a** at the top of the pipeline **b** at the bottom of the pipeline

area around the pipeline are shown in Figs. 18 and 19. Figures 18 and 19 show that case (6) results in less liquefaction potential around the pipeline.

5 Conclusion

Liquefaction of soil around a buried pipeline under earthquake loading is investigated in this study applying the mesh-free local RBF-DQ method. Using a multilayer node distribution in the computational domain, the effects of various physical parameters of the soil such as the permeability of the soil coefficient (k) and unit weight (γ) of the soil along with different shapes and locations of the trench layer are studied. From the liquefaction potential contours and pore pressure profiles, the following results are concluded:

(a) With increase in permeability of soil, the accumulative excess pore pressure generation reduces. Hence,

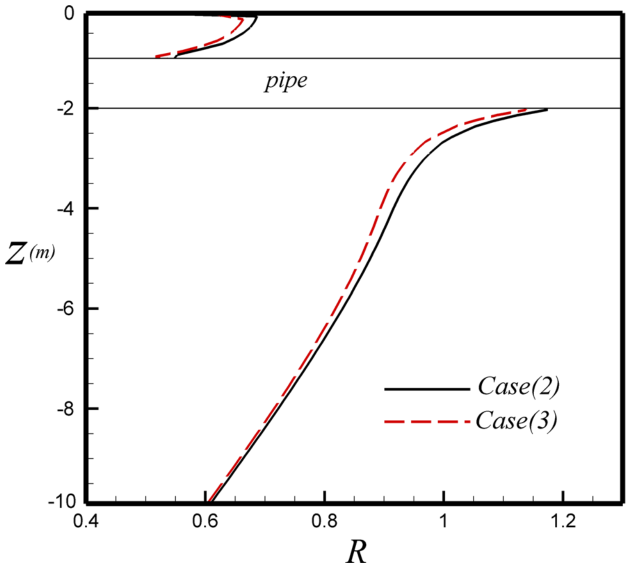

Fig. 17 Variation of R along the vertical centerline in the solution domain for different trapezoidal trench layers

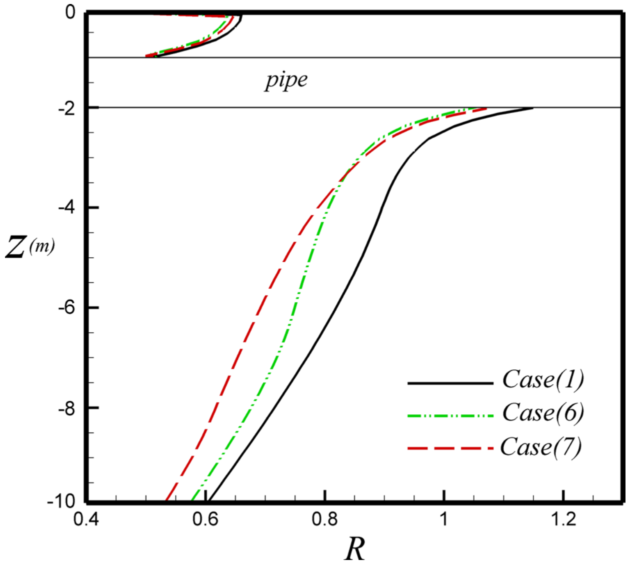

Fig. 18 Variation of R along the vertical centerline in the solution domain for different trench layer locations

increase in the permeability coefficient causes the values of R to reduce.

(b) As the distance from the trench layer increases, the effect of trench layer diminishes.

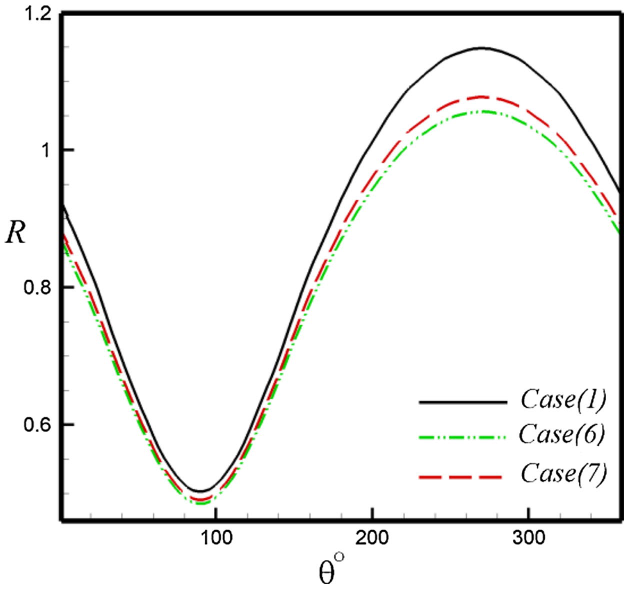

Fig. 19 Variation of R around the pipeline at various angular locations

(c) The trench layer with higher unit weight has a significant effect on the decrease in the liquefaction potential inside the trench area.

(d) Increase in the width of the trench layer has no significant effect on the accumulative excess pore pressure generation.

(e) The effect of changing depth of the trench layer is more considerable than the effect of its width.

(f) A triangular trench layer in which the base of the triangle is located at the deeper location of seabed causes less accumulative excess pore pressure.

References

1. Bararnia H, Jalaal M, Ghasemi M, Soleimani S, Ganji DD, Mohammadi F (2010) Numerical simulation of joule heating phenomenon using meshless RBF-DQ method. Int J Therm Sci 49:2117–2127
2. Bellman RE, Kashef BG, Casti J (1972) Differential quadrature: a technique for the rapid solution of nonlinear partial differential equations. J Comput Phys 10:40–52
3. Biot MA (1941) General theory of three-dimensional consolidation. J Appl Phys 12:155–164

4. Choobbasti AJ, Tavakoli H, Kutanaei SS (2014) Modeling and optimization of a trench layer location around a pipeline using artificial neural networks and particle swarm optimization algorithm. Tunn Undergr Space Technol 40:192–202
5. Ding H, Shu C, Tang DB (2005) Error estimates of local multiquadric-based differential quadrature (LMQDQ) method through numerical experiments. Int J Numer Meth Eng 63:1513–1529
6. Franke R (1982) Scattered data interpolation: tests of some methods. Math Comp 38:181–199
7. Hall WJ, O'Rourke TD (1991) Seismic behavior and vulnerability of pipelines. In: Cassaro MA (ed) Lifeline earthquake engineering. ASCE, New York, pp 761–773
8. Jalaal M, Soleimani S, Domairry G, Ghasemi E, Bararnia H, Mohammadi F, Barari A (2001) Numerical simulation of electric field in complex geometries for different electrode arrangements using meshless local MQ-DQ method. J Electrostat 69:168–175
9. Kansa EJ (1990) Multiquadrics—a scattered data approximation scheme with applications to computational fluid dynamics—I. Surface approximations and partial derivative estimates. Comput Math Appl 19:127–145
10. Kansa EJ (1990) Multiquadrics—a scattered data approximation scheme with applications to computational fluid dynamics—II. Solutions to parabolic, hyperbolic, and elliptic partial differential equations. Comput Math Appl 19:147–161
11. Karamitros DK, Bouckovalas GD, Kouretzis GP (2007) Stress analysis of buried steel pipelines at strike-slip fault crossings. Soil Dyn Earthq Eng 27:200–211
12. Kutanaei SS, Ghasemi E, Bayat M (2011) Mesh-free modeling of two-dimensional heat conduction between eccentric circular cylinders. Int J Phys Sci 6:4044–4052
13. Kutanaei SS, Roshan N, Vosoughi A, Saghafi S, Barari A, Soleimani S (2012) Numerical solution of stokes flow in a circular cavity using mesh-free local RBF-DQ. Eng Anal Bound Elem 36:633–638
14. Liu GR, Liu MB (2003) Smoothed particle hydrodynamics: a mesh free particle method. World Scientific Publishing Co. Pte. Ltd., Singapore
15. Liu WK, Jun S, Zhang YF (1995) Reproducing kernel particle methods. Int J Numer Methods Fluids 20:1081–1106
16. Maotian L, Xiaoling Z, Qing Y, Ying G (2009) Numerical analysis of liquefaction of porous seabed around pipeline fixed in space under seismic loading. Soil Dyn Earthq Eng 29:855–864
17. Matsui K (1982) Pressure and stress distribution around a pipeline buried in a poro-elastic seabed, PhD dissertation, University of Houston
18. O'Rourke TD, Hamada M (1992) Case studies of liquefaction and lifeline performance during past earthquakes: technical report NCEER-92-0002, vol 2. National Center for Earthquake Engineering Research, State University of New York at Buffalo, NY
19. Seed HB, Rahman MS (1978) Wave-induced pore pressure in relation to ocean floor stability of cohesionless soils. Mar Geotechnol 3:123–150
20. Seed HB, Martin PP, Lysmer J (1976) Pore-water pressure changes during soil liquefaction. J Geotech Eng Div 102:323–346
21. Shu C, Richards BE (1992) Application of generalized differential quadrature to solve two-dimension incompressible NaviereStokes equations. Int J Numer Meth Fluids 15:791–798
22. Shu C, Ding H, Yeo KS (2003) Local radial basis function-based differential quadrature method and its application to solve two dimensional incompressible Navier– Stokes equations. Comput Methods Appl Mech Eng 192:941–954
23. Shu C, Ding H, Chen HQ, Wang TG (2005) An upwind local RBF-DQ method for simulation of in viscid compressible flows. Comput Methods Appl Mech Eng 194:2001–2017
24. Sladek V, Sladek J, Tanaka M, Zhang CH (2005) Transient heat conduction in anisotropic and functionally grade media by local integral equations. Eng Anal Bound Elem 29:1047–1065
25. Sladek J, Sladek V, Hellmich C, Eberhardsteiner J (2007) Heat conduction analysis of 3-D axisymmetric and anisotropic FGM bodies by meshless local Petrov-Galerkin method. Comput Mech 39:323–333
26. Soleimani S, Jalaal M, Bararnia H, Ghasemi E, Ganji DD, Mohammadi F (2010) Local RBF-DQ method for two-dimensional transient heat conduction problems. Int Commun Heat Mass Transfer 37:1411–1418
27. Soleimani S, Ganji DD, Ghasemi E, Jalaal M, Bararnia H (2011) Meshless local RBF-DQ for 2D heat conduction: a comparative study. Therm Sci 15:117–121
28. Soleimani S, Qajarjazi A, Bararnia H, Barari A, Domairry G (2011) Entropy generation due to natural convection in a partially heated cavity by local RBF-DQ method. Meccanica 46:1023–1033
29. Sumer B, Hatipoglu F, Fredsøe J, Hansen N (2006) Critical flotation density of pipelines in soils liquefied by waves and density of liquefied soils. J. Waterway, Port, Coastal, Ocean Eng. 132, SPECIAL ISSUE: Liquefaction around marine structures. Processes and Benchmark Cases pp 252–265
30. Trautmann CH, O'Rourke TD, Kulhawy FD (1985) Uplift force-displacement response of buried pipe. J Geotech Eng 111:1061–1076
31. Xuan ZC, Zhang XK (2008) Simulation of Stokes flow over microelectrodes with least-squares meshfree method. Simul Model Pract Theory 16:294–314
32. Zhiying X (1981) An evaluation method of pore pressure during earthquake. J Hydraul Eng 4:68–73